Simultaneously Integrating Single Atomic Cobalt Sites and Co_9S_8 Nanoparticles into Hollow Carbon Nanotubes as Trifunctional Electrocatalysts for Zn–Air Batteries to Drive Water Splitting

Yizhe Li, Rui Cao, Longbin Li, Xiannong Tang, Tinglin Chu, Bingyu Huang, Kai Yuan, and Yiwang Chen**

The development of rechargeable metal–air batteries and water electrolyzers are highly constrained by electrocatalysts for the oxygen reduction reaction (ORR), oxygen evolution reaction (OER), and hydrogen evolution reaction (HER). However, the construction of efficient trifunctional electrocatalysts for ORR/OER/HER are highly desirable yet challenging. Herein, hollow carbon nanotubes integrated single cobalt atoms with Co_9S_8 nanoparticles (CoSA + Co_9S_8/HCNT) are fabricated by a straightforward in situ self-sacrificing strategy. The structure of the CoSA + Co_9S_8/HCNT are verified by X-ray absorption spectroscopy and aberration-corrected scanning transmission electron microscopy. Theoretical calculations and experimental results embrace the synergistic effects between Co_9S_8 nanoparticles and single cobalt atoms through optimizing the electronic configuration of the CoN_4 active sites to lower the reaction barrier and facilitating the ORR, OER, and HER simultaneously. Consequently, rechargeable liquid and all-solid-state flexible Zn–air batteries based on CoSA + Co_9S_8/HCNT exhibit remarkable stability and excellent power density of 177.33 and 51.85 mW cm^{-2}, respectively, better than Pt/C + RuO_2 counterparts. Moreover, the as-fabricated Zn–air batteries can drive an overall water splitting device assembled with CoSA + Co_9S_8/HCNT and achieve a current density of 10 mA cm^{-2} at a low voltage of 1.59 V, also superior to Pt/C + RuO_2. Therefore, this work presents a promising approach to an efficient trifunctional electrocatalyst toward practical applications.

Fuel cells, rechargeable metal–air batteries as well as electrochemical water splitting are widely recognized as efficient technologies for energy storage and conversion.[1–3] The oxygen reduction reaction (ORR), oxygen evolution reaction (OER), and hydrogen evolution reaction (HER) are the most critical electrochemical procedures for these energy-related technologies.[4–6] In practical applications, these reactions usually suffer problems of kinetic sluggishness and insufficient activity.[7,8] Noble metal based electrocatalysts (i.e., Ru/Ir oxides and Pt/C) are considered as the most efficient electrocatalysts for above electrochemical processes to date.[9,10] However, the scalable applications of noble metal based electrocatalysts are heavily impeded by their scarcity, high cost, and insufficient durability.[11–13] Therefore, the development of high-activity, durable, and inexpensive nonprecious metal electrocatalysts (NPMCs) as substitutes for noble metal electrocatalysts is of great significance.[14–18]

Numerous investigations have been devoted to explore NPMCs. Heteroatom-doped carbons, transition metal–nitrogen–carbon (M—N—C, M = Fe, Co, Cu, and Mn, etc.), metallic oxides/chalcogenides/carbides/nitrides have been evaluated as robust electrocatalysts with activity comparable to noble metals.[19–24] Among these materials, M—N—C electrocatalysts are recognized as one of the most active electrocatalysts in the electrocatalytic reaction processes.[25–28] Previous works have demonstrated that Co—N—C can act as trifunctional electrocatalyst toward ORR/OER/HER.[29–31] However, its catalytic activity is not satisfactory and needs to be further improved.[32,33]

On the other hand, thanks to the vast array of electronic structures and intrinsic physical properties, transition metal chalcogenides (TMCs) hold promise in the field of electrocatalysis, and have received extensive attention.[34–36] However, single TMC based electrocatalysts rarely meet the catalytic needs of different electrochemical reactions simultaneously. Introducing

Y. Li, L. Li, X. Tang, T. Chu, B. Huang, Prof. K. Yuan, Prof. Y. Chen
College of Chemistry/Institute of Polymers and Energy Chemistry
Nanchang University
999 Xuefu Avenue, Nanchang 330031, China
E-mail: kai.yuan@ncu.edu.cn; ywchen@ncu.edu.cn

Dr. R. Cao
Stanford Synchrotron Radiation Lightsource (SSRL)
SLAC National Accelerator Laboratory
Menlo Park, CA 94025, USA

Prof. Y. Chen
Institute of Advanced Scientific Research (iASR)
Jiangxi Normal University
99 Ziyang Avenue, Nanchang 330022, China

The ORCID identification number(s) for the author(s) of this article can be found under https://doi.org/10.1002/smll.201906735.

active sites with different functions is also supposed to an valid strategy for improving trifunctional catalytic activity of TMCs notwithstanding, it cannot achieve high activity by simply mixing different active sites together.[37] Therefore, the integration of various functional active sites to synergistically improve catalytic activity toward efficient trifunctional electrocatalysis is highly desired.

Herein, hollow carbon nanotube integrated single cobalt atoms with Co_9S_8 nanoparticles (CoSA + Co_9S_8/HCNT) is fabricated by an in situ self-sacrificing strategy. The structure of as-prepared CoSA + Co_9S_8/HCNT was identified by aberration-corrected high-resolution scanning transmission electron microscopy and synchrotron X-ray absorption spectroscopy. The unique structure enables CoSA + Co_9S_8/HCNT to act as efficient trifunctional electrocatalysts for ORR, OER, and HER. The CoSA + Co_9S_8/HCNT displays favorable ORR/OER activity and the potential difference (ΔE) between $E_{j=10}$ (potential at 10 mA cm^{-2} for OER) and $E_{1/2}$ (half wave potential of ORR) is 0.705 V, much smaller than that of Pt + RuO_2 (0.777 V). The liquid and all-solid-state flexible rechargeable Zn–air batteries assembled with CoSA + Co_9S_8/HCNT provide high peak power density of 177.33 and 51.85 mW cm^{-2}, respectively, superior to the devices based on Pt + RuO_2. Moreover, the water splitting electrolyzer assembled with CoSA + Co_9S_8/HCNT only needs to apply 1.59 V to achieve a current density of 10 mA cm^{-2}. Theoretical calculations reveal that the electronic configuration of CoN_4 could be optimized significantly by Co_9S_8 nanoparticles, thus reducing the reaction barrier as well enhancing the kinetic of adsorption–desorption of intermediates. Our work presents a straightforward approach to produce highly efficient trifunctional electrocatalyst toward practical applications.

The preparation of CoSA + Co_9S_8/HCNT is schematically illustrated in (**Figure 1**a). First, ZnS nanorods were use as templates for the growth of ZIF-67 to produce ZnS/ZIF-67. Followed by coating polydopamine (PDA), ZnS/ZIF-67-PDA was obtained. Finally, CoSA + Co_9S_8/HCNT were prepared by direct pyrolysis of ZnS/ZIF-67-PDA precursors at 1000 °C, for detailed experimental procedures see Supporting Information. During the pyrolysis process, the self-sacrificing ZnS nanorod templates were reduced to metallic Zn vapor and simultaneously saved as sulfur source. At the same time, ZIF-67 can act as the source of Co and N to form CoN_4 sites and is partially sulfurated to form Co_9S_8 nanoparticles. Meanwhile, the coated PDA layer was converted into carbon frameworks to connect the ZIF-67-derived carbon to generate hollow nanotubular structure. For comparison, ZnS-PDA (PDA-coated ZnS), ZIF-67, ZnS/ZIF-67, and ZIF-67-PDA (PDA-coated ZIF-67) were also prepared and carbonized at 1000 °C, the obtained products

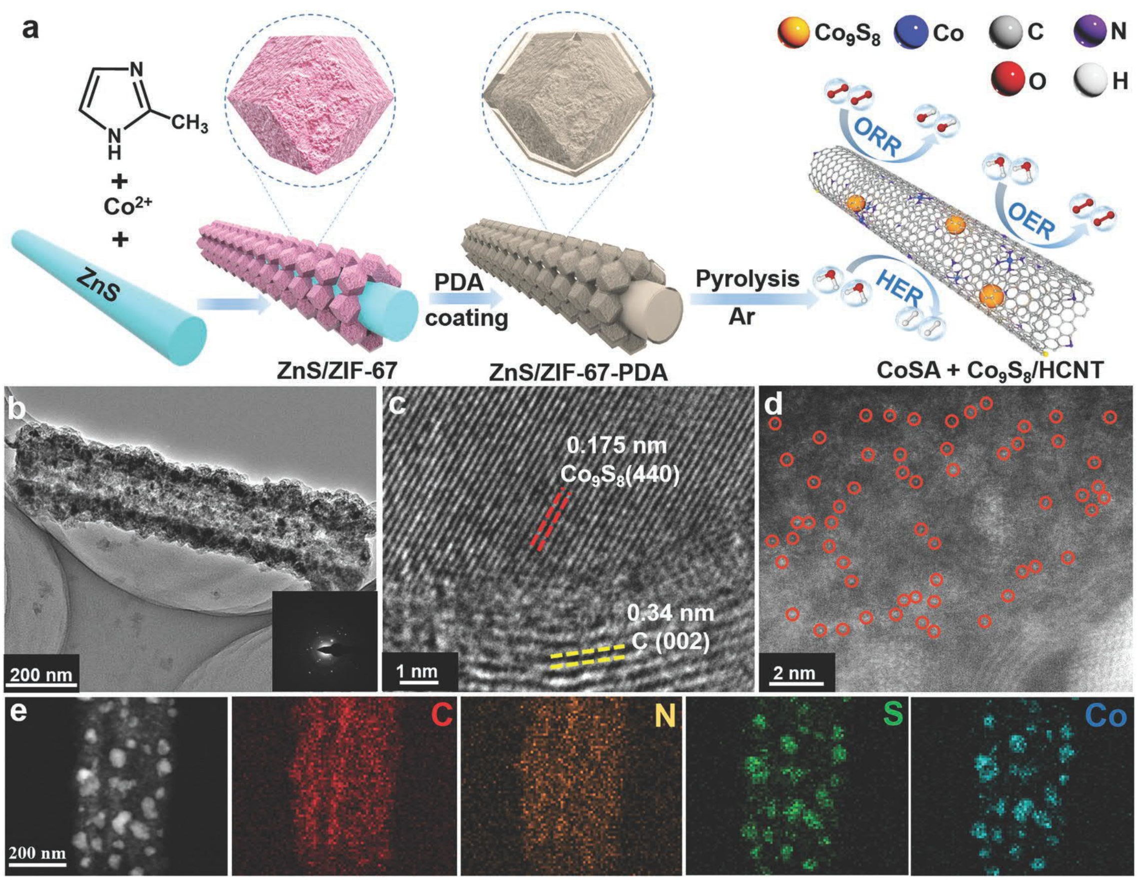

Figure 1. a) Schematics of the preparation of CoSA + Co_9S_8/HCNT trifunctional electrocatalyst. b) TEM image, inset is SAED pattern. c) HRTEM image. d) Aberration-corrected HADDF-STEM image (single Co atoms are highlighted by orange circles). e) HADDF-STEM and corresponding elemental mapping images of CoSA + Co_9S_8/HCNT.

were denoted as C-ZnS, C-ZIF-67, C-ZnS/ZIF-67, and C-ZIF-67-PDA, respectively.

The morphologies of the samples during the synthetic processes were characterized by electron microscopy. The diameter of the ZnS nanorod is about 300 nm, as shown in scanning electron microscopy and transmission electron microscopy (TEM) images (Figures S1 and S2, Supporting Information). The ZIF-67 nanocrystals homogeneously grew on the ZnS nanorods (Figure S3, Supporting Information), and still kept the nanorod morphology after coating a thin layer of PDA (Figures S4 and S5, Supporting Information). After carbonization, the ZnS nanorods were self-sacrificed to form a tubular structure (Figure 1b and Figure S6, Supporting Information) and act as the sulfur source for the formation of Co_9S_8 nanoparticles. The selected area electron diffraction (SAED) image (inset of Figure 1b) reveals the polycrystalline structure of Co_9S_8 nanoparticles. The high-resolution TEM image demonstrated that Co_9S_8 nanoparticles were covered by graphitic carbon layers (Figure S7, Supporting Information). The graphitic carbon layers can prevent the Co_9S_8 nanoparticles from leaching out to the electrolyte, thereby improving the stability.[38–40] The lattice fringes with d-spacing of 0.175 and 0.34 nm correspond to the (440) plane of Co_9S_8 and the (002) plane of the graphitic carbon layers, respectively (Figure 1c). Furthermore, bright dots (highlighted in orange circles) observed by the aberration-corrected high-angle annular dark-field scanning transmission electron microscopy (HAADF-STEM) images intuitively hinted the existence of single Co atoms (Figure 1d and Figure S8, Supporting Information). The HAADF-STEM and corresponding energy-dispersive spectroscopy mapping images revel the uniform distribution of Co, C, N, and S throughout the hollow carbon nanotubes (Figure 1e). The uniform dispersion and simultaneous presence of Co and S indicate the homogeneous composition of the nanoparticles. The above results revealed the coexistence of single Co atoms and Co_9S_8 nanoparticles in the as-prepared CoSA + Co_9S_8/HCNT.

The crystal structure evolution of the samples during the preparation of CoSA + Co_9S_8/HCNT were investigated by X-ray diffraction (XRD). The XRD pattern of ZnS/ZIF-67 contains diffraction peaks of ZnS and ZIF-67 (Figure S9a, Supporting Information), which means that ZIF-67 nanoparticles have successfully grown on ZnS nanorods. The peak intensity becomes weaker after coating with PDA. After carbonization, the peaks for CoSA + Co_9S_8/HCNT located at 15°, 30°, 47°, and 52° are attributed to the (111), (311), (511), and (440) planes of Co_9S_8 (JCPDS 65-6801), respectively, indicating the formation of the Co_9S_8. Since defective carbons are considered as active sites for electrocatalysis, Raman spectra were used to study the defect degree of the as-prepared electrocatalysts (Figure S9b, Supporting Information). The two broad peaks at 1345 and 1582 cm^{-1} represent D (disordered or defective carbon) and G (sp^2 hybridized carbon) bands, respectively. The I_D/I_G ratio for CoSA + Co_9S_8/HCNT (1.18) is higher than all reference samples, suggesting more defect sites in CoSA + Co_9S_8/HCNT.

The porous structure and specific surface area of electrocatalysts are significant parameters during catalytic process. N_2 adsorption–desorption isotherms were recorded to study the porous structure of the electrocatalysts (Figure S10, Supporting Information). All the electrocatalysts display a typical type-IV isotherm, which contain obvious gas uptake at low pressure ($P/P_0 < 0.01$) and hysteresis loop at high pressure, revealing the presence of both micro- and mesopores.[41] CoSA + Co_9S_8/HCNT displays the highest Brunauer–Emmett–Teller (BET) surface area is 635.88 m^2 g^{-1} (Table S1, Supporting Information). A larger specific surface area is usually favorable for improving the catalytic activity of electrocatalysis due to the exposure of more active sites. The pore size distribution profile of CoSA + Co_9S_8/HCNT displays main peaks at 0.94, 4.08, and 7.53 nm, proving the hierarchical porous structure (Figure S11, Supporting Information), which leads to a fast mass diffusion and a favorable accessibility of the active sites/electrolytes thus improve catalytic activity.

The chemical composition and the bonding structure of the as-prepared electrocatalysts were investigated by X-ray photoelectron spectroscopy (XPS). The survey XPS spectrum of CoSA + Co_9S_8/HCNT indicates the existence of Co, N, C, and S (Figure S12a, Supporting Information). The corresponding atomic percentages for Co, N, and S are 2.90%, 1.82%, and 4.92%, respectively (Figure S12b–f, Supporting Information). The high-resolution C 1s spectra of CoSA + Co_9S_8/HCNT (Figure S13a, Supporting Information) contain four peaks assigned to C = O (286.6 eV), C—N (285.4 eV), C—C (284.8 eV), and C—S (283.9 eV).[42] The N 1s spectrum was deconvoluted into five peaks at 404, 401.2, 400.1, 399.2, and 398.4 eV, corresponding to the oxidized N, graphitic N, pyrrolic N, Co-N, and pyridinic N, respectively (Figure S14a, Supporting Information).[43] Co-N, pyridinic N, and graphitic N are usually considered as important species for ORR/OER/HER.[44] In addition, pyridinic N and pyrrolic N can stabilize the metal Co center to ensure the formation of single atomic CoN_4 structure.[45] According to the N 1s XPS spectra of the electrocatalysts (Figure S14a–e, Supporting Information), the corresponding percentage distribution of nitrogen species are statistically shown in Figure S14f, Supporting Information. The N species in CoSA + Co_9S_8/HCNT are mainly pyridinic and graphitic nitrogen, which could lead to improved catalytic activity. The deconvoluted S 2p spectra (Figure S15a, Supporting Information) of CoSA + Co_9S_8/HCNT displays peaks of Co—S at 161.9 and 162.8 eV, corresponding to S $2p_{3/2}$ and S $2p_{1/2}$, respectively.[42] The high-resolution Co 2p spectra (Figure S16a, Supporting Information) can be deconvoluted into Co $2p_{3/2}$ (782.4 and 778.8 eV) and Co $2p_{1/2}$ (793.8 and 798.5 eV), confirming the formation of Co_9S_8.[38]

The X-ray absorption fine structure (XAFS) measurements were further conducted to confirm the coordination geometry of CoSA + Co_9S_8/HCNT. The Co K-edge X-ray absorption near-edge structure (XANES) spectra of CoSA + Co_9S_8/HCNT (**Figure 2**a) show that the pre-edge of CoSA + Co_9S_8/HCNT is similar to Co porphyrin but quite different from Co foil, demonstrating a structure component similar to Co porphyrin with CoN_4 in CoSA + Co_9S_8/HCNT. For the C K-edge spectrum of CoSA + Co_9S_8/HCNT, the peaks located at 285.1 and 292.5 eV (Figure S17a, Supporting Information) assign to aromatic carbon species and sp^3 hybridized σ^* band, respectively.[46] The resonance shoulder peak at around 287.4 eV originate from the Co—N—C bond in the CoSA + Co_9S_8/HCNT.[47] The three peaks at 399.2, 403.3, and 408.9 eV in the N K-edge spectrum correspond to pyridinic N, graphitic N, and the σ^* C—N bond,

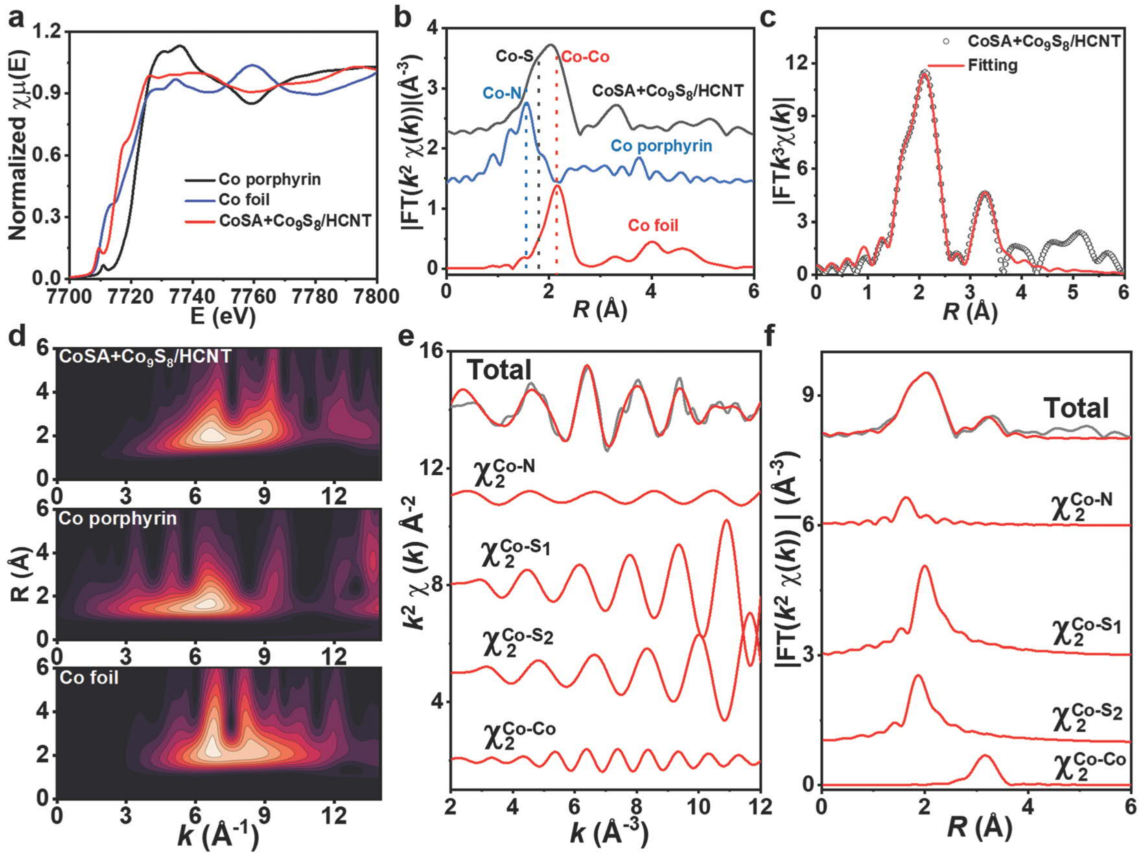

Figure 2. a) Co K-edge XANES spectra, and b) corresponding Fourier transform (FT) of k^2-weighted Co K-edge EXAFS spectra for CoSA + Co_9S_8/HCNT, Co porphyrin, and Co foil samples. c) The EXAFS fitting curves of CoSA + Co_9S_8/HCNT in R space. d) Wavelet transform (WT) of Co K-edge k^3-weighted EXAFS for CoSA + Co_9S_8/HCNT, Co porphyrin, and Co foil samples. Co K-edge EXAFS of CoSA + Co_9S_8/HCNT in e) k and f) R spaces.

respectively (Figure S17b, Supporting Information).[47] For the S L-edge XANES spectrum (Figure S17c, Supporting Information), the three typical peaks between 163 and 167 eV correspond to C—S—C bonds.[48]

To obtain the atomic coordination environment of the Co atoms in CoSA + Co_9S_8/HCNT, the extended X-ray absorption fine structure (EXAFS) spectra were further studied. The Fourier transformed (FT) k^2-weighted phase uncorrected Co K-edge EXAFS spectra is demonstrated in Figure 2b. The peaks at 1.79 and 2.15 Å can be attributed to the Co—S and Co—Co single scattering paths, respectively, revealing the existence of Co_9S_8. The Co—N signal at 1.45 Å originates from CoN_4 structure on the carbon matrix. The EXAFS R space fitting curves in Figure 2c show that the combined magnitudes of the paths originated from Co_9S_8 and CoN_4 fit well with the structural components of CoSA + Co_9S_8/HCNT. EXAFS wavelet transform (WT) analysis supplies radial distance and k space resolution to discriminate the backscattering atoms.[49] According to the result of FT k^3-weighted EXAFS spectra, the WT analyses display two prominent features centered at ≈6.5 and 8.5 $Å^{-1}$ (Figure 2d, middle and bottom graph), which are comparable to the features of Co—N found in Co porphyrin and Co—Co in the cobalt foil, respectively. The quantitative least-squares EXAFS curve fitting further reveals the coordination configurations in CoSA + Co_9S_8/HCNT. Four backscattering paths including Co—N, Co—S_1, Co—S_2, and Co—Co were adopted to analyze the EXAFS spectrum of CoSA + Co_9S_8/HCNT (Figure 2e,f and Table S2, Supporting Information). The best fitting analyses display a shoulder peak at 1.63 Å attributed to the Co—N first shell coordination. The main peak at 2.0 Å originates from Co—S_1 (1.98 Å) and Co—S_2 (1.87 Å) while the second shell peak at 3.2 Å results from Co—Co contribution. The phase-corrected fitting results' derived bond length for Co—N (≈1.97 Å) with corresponding coordination number is 4.0, consistent with a CoN_4 structure. The presence of Co_9S_8 was further supported by the two different sets of Co—S bonds, that is, Co—S_1 at 2.19 Å and Co—S_2 at 2.32 Å, in consistent with the co-presence of two different unit cells in Co_9S_8.[50] The coordination number for Co—S_1 and Co—S_2 are best fitted as 4.0 and 6.0, respectively. In summary, the XAFS analyses further support that the as-prepared hollow carbon nanotubes were integrated Co_9S_8 nanoparticles and single cobalt atoms with CoN_4 configuration.

The hierarchical porous structure and unique electronic structures as well as compositional merits of CoSA + Co_9S_8/HCNT are favorable for electrocatalytic processes. Linear sweep voltammetry (LSV) was first conducted with a rotating disk electrode (RDE) at 1600 rpm to investigate the catalytic activity toward ORR. The CoSA + Co_9S_8/HCNT prepared at 1000 °C exhibits the maximal limited current density and the most positive half wave potential ($E_{1/2}$) of 0.855 V versus RHE (**Figure 3**a and Figure S18, Supporting Information). The

CoSA + Co_9S_8/HCNT is comparable to and even superior to most of advanced cobalt based ORR electrocatalysts reported so far (Table S3, Supporting Information). According to the Koutecky–Levich (K–L) plots, the electron transfer number (*n*) was determined to be 3.98 for CoSA + Co_9S_8/HCNT, confirming a four-electron pathway toward ORR (inset in Figure 3b). The corresponding Tafel slope (Figure 3c) for CoSA + Co_9S_8/HCNT (30 mV dec^{-1}) is much lower than that for Pt/C (78 mV dec^{-1}), indicating an excellent dynamic process. Furthermore, the rotating ring–disk electrode measurements were further carried out to investigate the *n* and hydrogen peroxide (HO_2^-) yield during ORR (Figure 3d and Figures S19 and S20, Supporting Information). The HO_2^- yield of CoSA + Co_9S_8/HCNT is less than 2% and the value of *n* is 3.99, which is coincident with the result obtained from the K–L plots, demonstrating again the excellent four-electron pathway selectively of CoSA + Co_9S_8/HCNT for ORR. The influence of SCN^- ion for ORR is investigated to illuminate the nature of single-atom CoN_4 sites. The SCN^- ion tends to attack metal-centered catalytic sites resulting in reduced catalytic activity.[51] After introducing 10 mM KSCN into the electrolyte, the $E_{1/2}$ of CoSA + Co_9S_8/HCNT was significantly decreased from 0.855 to 0.723 V, while the current density was reduced by almost half (Figure S21, Supporting Information). Therefore, it can be proved that CoN_4 in CoSA + Co_9S_8/HCNT play an important role toward ORR.

To investigate the intrinsic ORR activity of as-prepared electrocatalysts, we calculated electrochemically active surface area (ECSA) based on the double layer capacitance (C_{dl}). The CoSA + Co_9S_8/HCNT sample possesses the highest C_{dl} of 51.33 mF cm^{-2} (Figure S22, Supporting Information) and the corresponding ECSA is 251.49 m^2 g^{-1} (Table S4, Supporting Information). The CoSA + Co_9S_8/HCNT shows the highest kinetic current density normalized by EESA, indicating an excellent kinetic process (Figure S23, Supporting Information). The durability of CoSA + Co_9S_8/HCNT and Pt/C were evaluated by chronoamperometry at 0.7 V (vs RHE). After

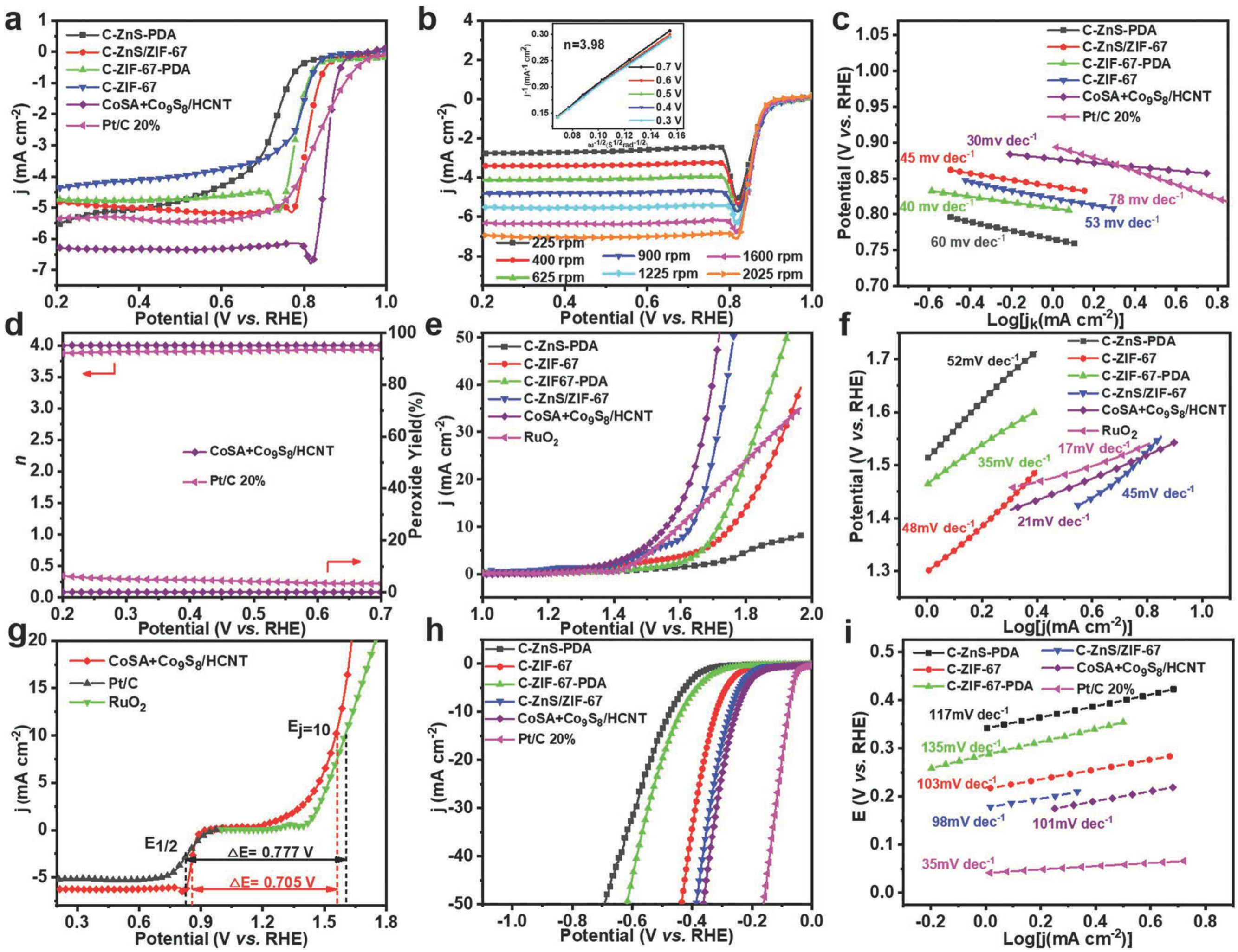

Figure 3. a) ORR polarization curves at 1600 rpm. b) LSV curves of CoSA + Co_9S_8/HCNT for ORR at different rotating rates, and inset is corresponding K–L plots. c) Corresponding Tafel slopes of C-ZnS-PDA, C-ZnS/ZIF-67, C-ZIF-67, C-ZIF-67-PDA, CoSA + Co_9S_8/HCNT, and Pt/C 20% for ORR. d) Electron transfer number (*n*) and HO_2^- yield for CoSA + Co_9S_8/HCNT and Pt/C 20%. e) OER polarization curves of as-prepared electrocatalysts at 1600 rpm. f) Corresponding Tafel slopes of the electrocatalysts for OER. g) LSV curves for both ORR and OER at 1600 rpm. h) HER polarization curves and i) Tafel slopes of the electrocatalysts for HER.

12 h, the current density of CoSA + Co_9S_8/HCNT can still maintain 98.4% (Figure S24, Supporting Information), much better than Pt/C (89.5%). The tolerance of methanol was further evaluated by adding 3 M methanol into electrolyte during the chronoamperometric measurements. After the addition of methanol, a dramatic current density reduction can be observed for Pt/C, demonstrating that Pt/C is intensively inactivated (Figure S25, Supporting Information). In contrast, inconspicuous current density decay can be observed for CoSA + Co_9S_8/HCNT, confirming its robust resistance to methanol crossover. The excellent durability of the as-prepared CoSA + Co_9S_8/HCNT verified it is a promising electrocatalyst for practical application.

The CoSA + Co_9S_8/HCNT also exhibits prominent catalytic activity toward OER to achieve an application in rechargeable Zn–air batteries. The LSV curves reveal that CoSA + Co_9S_8/HCNT prepared at 1000 °C requires the lowest potential of 1.56 V versus RHE to attain a 10 mA cm^{-2} current density ($E_{j=10}$) among all the samples, suggesting the best catalytic ability (Figure 3e and Figure S26, Supporting Information). Such low potential is comparable to and even lower than most OER electrocatalysts reported to date (Table S5, Supporting Information). In addition, CoSA + Co_9S_8/HCNT also displays a low Tafel slop of 21 mV dec^{-1}, very close to the value of benchmark RuO_2 (17 mV dec^{-1}) (Figure 3f). As shown in Figure S27, Supporting Information, after injecting 10 mM KSCN into the electrolyte, the overpotential increased more than 140 mV, demonstrating CoN_4 in CoSA + Co_9S_8/HCNT is crucial for OER. The bifunctional activity was further assessed by ΔE ($E_{j=10}$–$E_{1/2}$). The ΔE for CoSA + Co_9S_8/HCNT is 0.705 V, much smaller than the mixture of Pt/C and RuO_2 (0.777 V, Figure 3g). Moreover, the ΔE for CoSA + Co_9S_8/HCNT outperforms most of the previously reported bifunctional electrocatalysts (Table S6, Supporting Information), suggesting its good prospect for rechargeable Zn–air batteries.

In addition to the excellent ability of bifunctional catalysis for OER and ORR, the CoSA + Co_9S_8/HCNT also shows high activity for HER. The LSV curves were obtained by using RDE in a N_2-saturated 1.0 M KOH electrolyte. The LSV curves in Figure 3h show that CoSA + Co_9S_8/HCNT prepared at 1000 °C possesses the highest catalytic activity with an overpotential of 250 mV at 10 mA cm^{-2}, close to commercial Pt/C (Figure 3h and Figure S28, Supporting Information). The Tafel slope for CoSA + Co_9S_8/HCNT is as low as 101 mV dec^{-1} (Figure 3i), it demonstrates a favorable kinetic process for HER. To verify the effect of single-atom CoN_4 in HER, 10 mM KSCN is also introduced. The overpotential displays a significant negative shift of 210 mV at 10 mA cm^{-2}, attesting CoN_4 provided a great contribution in HER (Figure S29, Supporting Information). The minimal contact angle confirms the best hydrophilicity of CoSA + Co_9S_8/HCNT (Figure S30, Supporting Information), which is beneficial to the accessibility of the electrolyte. The electrode/electrolyte interface resistance can be reduced due to increased hydrophilicity by optimizing surface wettability. The electrochemical impedance tests show the lowest charge transfer resistance of CoSA + Co_9S_8/HCNT, which is consistent with hydrophilicity analysis, confirming a more favorable electron transfer process (Figure S31, Supporting Information). All these results demonstrate the remarkable electrocatalytic performance of CoSA + Co_9S_8/HCNT for HER in alkaline electrolyte.

Due to the superior trifunctional catalytic activity toward ORR, OER, and HER, CoSA + Co_9S_8/HCNT was applied to rechargeable Zn–air batteries and water electrolyzer to investigate its practical application. Primary liquid Zn–air battery was first assembled and the construction is illustrated in **Figure 4**a and Figure S32, Supporting Information. The device based on Pt/C was also assembled for comparison. The polarization and corresponding power density curves are presented in Figure 4b. The Zn–air battery constructed with CoSA + Co_9S_8/HCNT displays an open circuit voltage of 1.45 V. The peak power density (177.33 mW cm^{-2}) is superior to the Zn–air battery assembled by using Pt/C as cathode (91.15 mW cm^{-2}). According to the long time galvanostatic discharge (Figure S33, Supporting Information), the Zn–air battery constructed with CoSA + Co_9S_8/HCNT displays a specific capacity of 788 mA h g^{-1} at 100 mA cm^{-2}, higher than that based on Pt/C (691 mA h g^{-1}), demonstrating that it is a promising substitute to noble metal based electrocatalysts. Discharge and charge polarization curves show that the gap between discharge and charge voltage of rechargeable Zn–air battery constructed with CoSA + Co_9S_8/HCNT (0.83 V) is smaller than that of Pt/C + RuO_2 (0.99 V) as cathode (Figure S34, Supporting Information). Long time galvanostatic discharge–charge cycling (Figure 4c) demonstrate a high round-trip efficiency of ≈63.9%, which is comparable to and even better than most advanced catalysts reported so far (Table S7, Supporting Information). Moreover, the discharging–charging voltage gap for Zn–air battery based on CoSA + Co_9S_8/HCNT exhibits much smaller change than device based on Pt/C + RuO_2 (Figure 4c). This result further confirms the prominent durability of CoSA + Co_9S_8/HCNT.

Because of the increasing demand for wearable and flexible devices, all-solid-state flexible rechargeable Zn–air batteries were further assembled by using CoSA + Co_9S_8/HCNT as air cathode (Figure 4d). The open circuit voltage of the as-fabricated device is ≈1.4 V (Figure S35, Supporting Information). The peak power density of the flexible Zn–air battery based on CoSA + Co_9S_8/HCNT can reach 51.85 mW cm^{-2} (Figure S36, Supporting Information), higher than the device by using Pt/C + RuO_2 as air cathode (43.76 mW cm^{-2}). Discharge and charge polarization curve of the flexible Zn–air battery assembled with CoSA + Co_9S_8/HCNT exhibits a higher discharging voltage and a smaller charging voltage compared with Pt/C + RuO_2 based battery (Figure S37, Supporting Information). The photograph inset in Figure S37, Supporting Information, shows the LED can be powered by two flexible Zn–air batteries in series. The galvanostatic discharge–charge cycling measurements were also collected at a 1 mA cm^{-2} to verify the durability of CoSA + Co_9S_8/HCNT. The flexible Zn–air battery based on CoSA + Co_9S_8/HCNT maintains a stable discharge–charge potential after long time cycling (Figure 4e). Moreover, negligible voltage change was observed even under various bending conditions (Figure S38, Supporting Information). These results confirm the superb stability of CoSA + Co_9S_8/HCNT, enables it as a promising air cathode for all-solid-state flexible rechargeable Zn–air battery.

Considering the robust OER and HER performance of CoSA + Co_9S_8/HCNT (Table S8, Supporting Information),

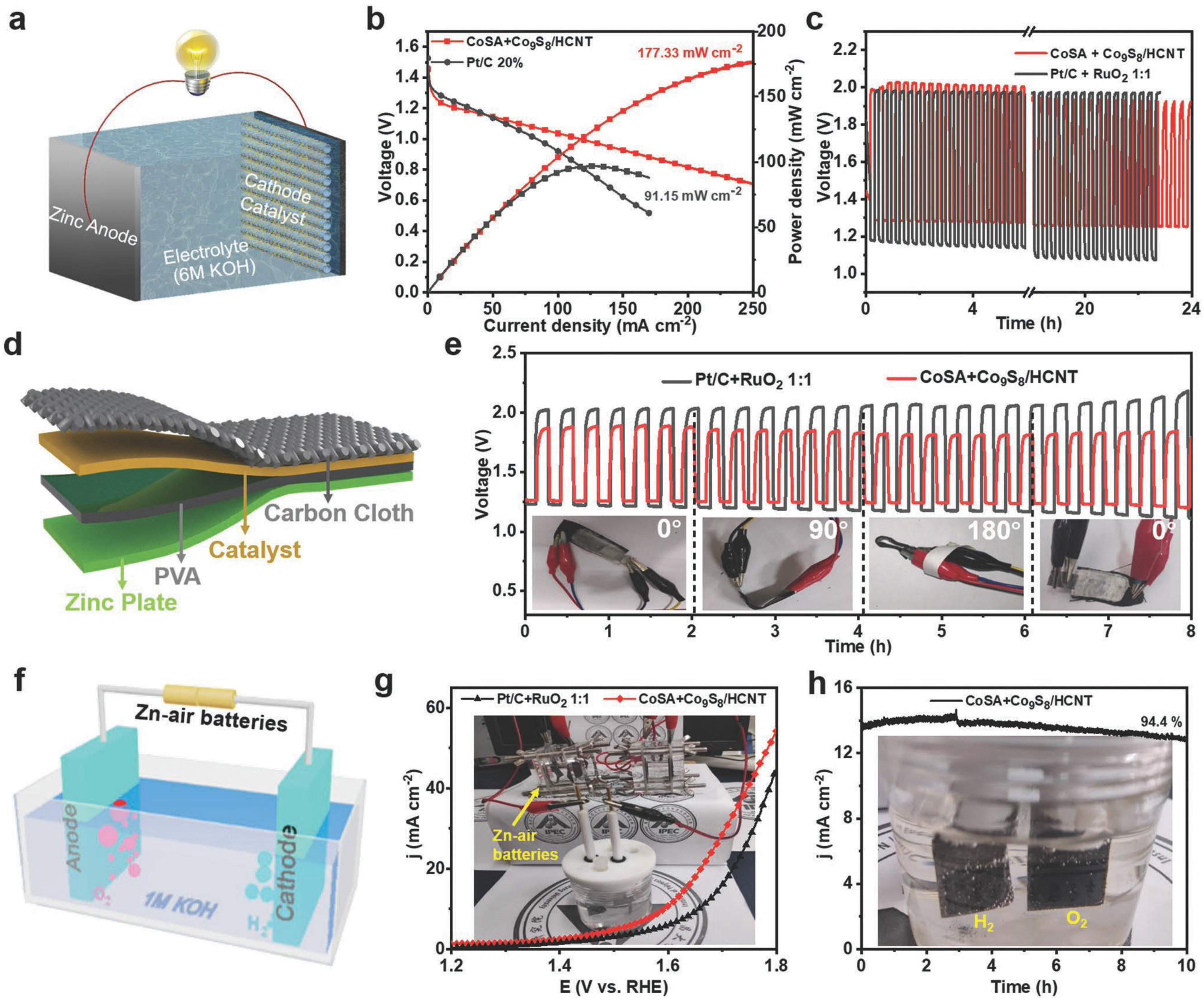

Figure 4. a) The schematic illustration of Zn–air battery. b) Polarization and power density curves of Zn–air batteries based on CoSA + Co_9S_8/HCNT and Pt/C. c) Galvanostatic discharge–charge cycling profiles of the liquid Zn–air batteries assembled with CoSA + Co_9S_8/HCNT or Pt/C + RuO_2 mixture at 5 mA cm^{-2}. d) Schematic diagram of the all-solid-state flexible Zn–air battery. e) Discharge–charge cycling profiles of the all-solid-state flexible Zn–air batteries CoSA + Co_9S_8/HCNT and Pt/C + RuO_2 at 1 mA cm^{-2}. f) Schematic diagram of self-power water splitting electrolyzer. g) LSV curve of the CoSA + Co_9S_8/HCNT electrodes and inset is the photograph of self-power water splitting device. h) Chronoamperometric responses of CoSA + Co_9S_8/HCNT‖CoSA + Co_9S_8/HCNT cells at 1.6 V and inset is the image of electrodes during the electrolysis of water.

an overall water splitting system was further constructed and powered by CoSA + Co_9S_8/HCNT based Zn–air batteries. Two pieces of carbon paper with CoSA + Co_9S_8/HCNT loading of 1 mg cm^{-2} were served as the cathode and the anode to construct a water splitting system (Figure 4f). The LSV curves in Figure 4g demonstrates that CoSA + Co_9S_8/HCNT‖CoSA + Co_9S_8/HCNT cell only requires 1.59 V to achieve a current density of 10 mA cm^{-2}, much lower than Pt/C + RuO_2 (1.66 V). The inset in Figure 4g shows a self-powered water splitting device generates a large amount of gas during water splitting. Subsequently, we further reviewed the stability of the device by using the chronoamperometric response conducted at 1.6 V. The device displays a steady current density with an insignificant fluctuation caused by the generation of bubbles (Figure 4h). After continuous 10 h of water splitting, the current density still possesses a retention of 94.5%. Therefore, the CoSA + Co_9S_8/HCNT can be used as an efficient multifunctional electrocatalyst for overall water splitting system with superior durability.

Furthermore, to get an insight into the mechanisms of ORR, OER, and HER at atomic scale, density functional theory (DFT) calculations were employed. According to the experimental results, three models, that is, CoN_4, Co_9S_8, and CoN_4 + Co_9S_8, were constructed to illustrate the fundamental mechanism of CoSA + Co_9S_8/HCNT for ORR/OER/HER (**Figure 5**a and Figures S39–S41, Supporting Information). The CoN_4 is modeled by using CoN_4-doped graphene and the (110) plane is used to model Co_9S_8. The model of CoN_4 + Co_9S_8 (represent CoSA + Co_9S_8/HCNT) was constructed by encapsulating Co_9S_8 in single-atom CoN_4-doped graphene. The free energy diagrams (Figure 5b) indicate that the adsorption free energy of electron transfer

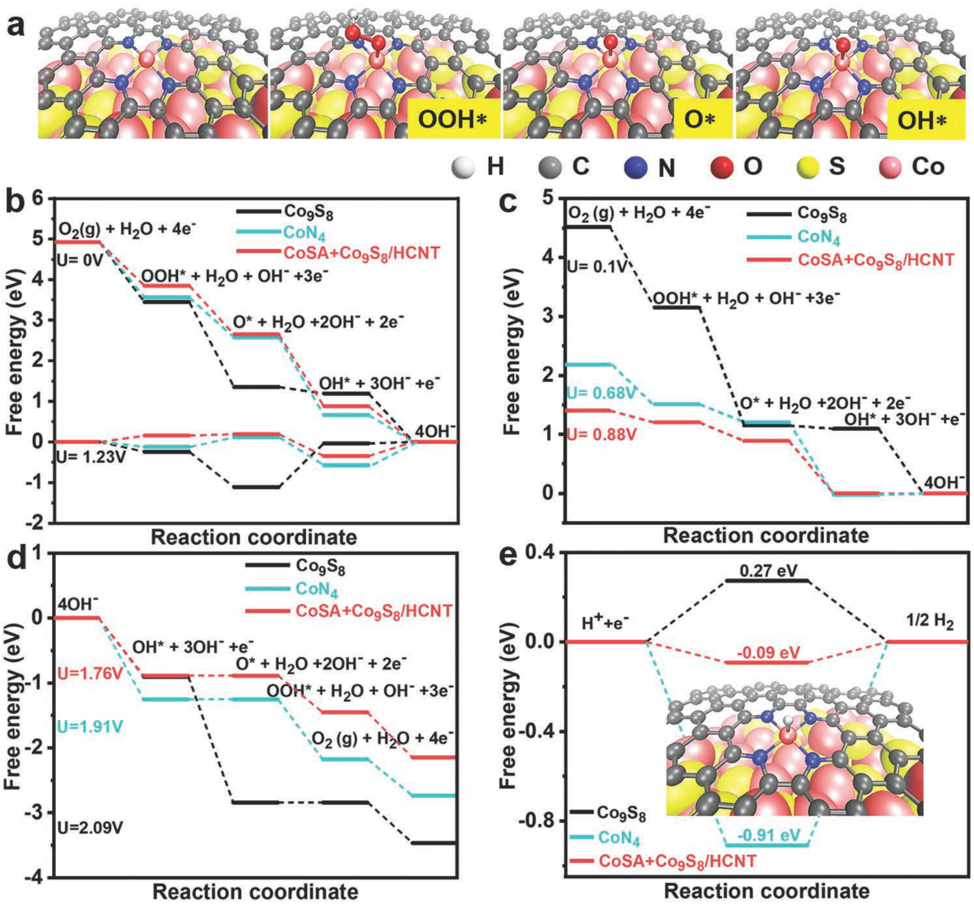

Figure 5. a) The models of adsorption configuration of ORR, OER on CoSA + Co_9S_8/HCNT. b) Free energy diagrams of Co_9S_8, CoN_4, and CoSA + Co_9S_8/HCNT at U = 0 V and U = 1.23 V. c) Free energy diagrams for the thermodynamic limiting potentials of ORR steps. d) Free energy diagrams for the thermodynamic limiting potentials of OER steps. e) Free energy diagrams of Co_9S_8, CoN_4, and CoSA + Co_9S_8/HCNT for HER and inset is the model of adsorption configuration of HER on CoSA + Co_9S_8/HCNT.

during all ORR processes are downhill at $U = 0$ V, which means that the reaction can proceed spontaneously (Table S9, Supporting Information). However, at a higher potential $U = 1.23$ V, the desorption process of OH* shows an obvious uphill trend, revealing that this step is the rate-determining step for CoN_4 and CoN_4 + Co_9S_8 (Table S10, Supporting Information). The CoN_4 + Co_9S_8 displays a smaller adsorption free energy (0.35 eV) than CoN_4 (0.57 eV) during OH* desorption, confirming that the presence of Co_9S_8 can facilitate the desorption of OH*. As shown in Figure 5c, for Co_9S_8, CoN_4, and CoN_4 + Co_9S_8, the thermodynamic limiting potentials of all ORR steps that ensures downhill in free energy are 0.1, 0.68, and 0.88 V, respectively, revealing superior ORR catalytic activity of CoSA + Co_9S_8/HCNT. The similar calculations are proposed to demonstrate OER performance. The thermodynamic limiting potential of OER for Co_9S_8, CoN_4, and CoN_4 + Co_9S_8 are 2.09, 1.91, and 1.76 V, respectively (Figure 5d), indicating the best OER performance of CoSA + Co_9S_8/HCNT caused by the synergistical interaction between Co_9S_8 and single-atom CoN_4 sites. The above results demonstrate that CoSA + Co_9S_8/HCNT possess the best activity for ORR/OER, which is coincident with the experimental results.

In order to further clarify the mechanism of CoSA + Co_9S_8/HCNT for HER, the chemisorption of hydrogen was also studied by DFT calculation. The H* adsorption free energy $|\Delta GH^*|$ values of Co_9S_8 and single-atom CoN_4 are 0.27 and –0.91 eV, respectively, while CoSA + Co_9S_8/HCNT displays a minimum value of –0.09 eV, manifesting the highest catalytic activity of CoSA + Co_9S_8/HCNT toward HER (Figure 5e). Therefore, the presence of Co_9S_8 can optimize the catalytic electronic configuration of the single-atom CoN_4 to synergistically lowering the barrier of ORR, OER, and HER simultaneously. The superiority of CoSA + Co_9S_8/HCNT as a trifunctional electrocatalyst is proved theoretically, also confirming its great potential in practical application.

In summary, a robust and efficient ORR, OER, and HER trifunctional electrocatalyst CoSA + Co_9S_8/HCNT was prepared by a facile in situ self-sacrificing strategy. The self-sacrificing ZnS nanorod templates were used to supply sulfur source and produce hollow carbon nanotubes with hierarchical porous structure. The aberration-corrected HAADF-STEM and XAFS analysis further verified the as-prepared CoSA + Co_9S_8/HCNT with hollow nanotube structure integrate single cobalt atoms with Co_9S_8 nanoparticles to synergistically facilitate ORR, OER, and HER. The potential application of CoSA + Co_9S_8/HCNT is investigated by rechargeable Zn–air batteries and overall water splitting devices. The rechargeable liquid Zn–air battery assembled with CoSA + Co_9S_8/HCNT demonstrated high power density of 177.33 mW cm^{-2} and remarkable durability. In addition, all-solid-state flexible rechargeable Zn–air battery can also deliver an impressed power density of 51.85 mW cm^{-2}. Moreover, the water splitting electrode for CoSA + Co_9S_8/HCNT required only 1.59 V to achieve 10 mA cm^{-2}. DFT calculation gives an insight to clarify the mechanism toward ORR/OER/HER, confirming that the interaction between Co_9S_8 and single-atom CoN_4 sites can optimize the electronic configuration of the active sites to synergistically lower the barrier of the reaction. Therefore, our work provides a straightforward approach to efficient and durable trifunctional electrocatalysts as substitute to noble metal based electrocatalysts for energy-related technologies.

Acknowledgements

Y.L. and R.C. contributed equally to this work. The authors acknowledge financial support from the National Natural Science Foundation of China (21704038, 51763018), the NSFC-DFG Joint Research Project (51761135114), the Natural Science Foundation of Jiangxi Province (20171ACB21009, 2018ACB21021, 20192BCB23001), the National Postdoctoral Program for Innovative Talents (BX201700112), and the China Postdoctoral Science Foundation (2018M632599). The authors thank Stanford Synchrotron Radiation Lightsource (SSRL) BL 7-3 for providing the beamtime.

Conflict of Interest

The authors declare no conflict of interest.

Keywords

electrocatalysts, nanoparticles, single atoms, water splitting, Zn–air batteries

Received: November 20, 2019
Revised: December 27, 2019
Published online: January 27, 2020

[1] X. X. Wang, M. T. Swihart, G. Wu, *Nat. Catal.* **2019**, *2*, 578.
[2] Z. P. Cano, D. Banham, S. Ye, A. Hintennach, J. Lu, M. Fowler, Z. Chen, *Nat. Energy* **2018**, *3*, 279.
[3] D. Wang, Q. Li, C. Han, Q. Lu, Z. Xing, X. Yang, *Nat. Commun.* **2019**, *10*, 3899.
[4] A. A. Gewirth, J. A. Varnell, A. M. DiAscro, *Chem. Rev.* **2018**, *118*, 2313.
[5] X. R. Wang, J. Y. Liu, Z. W. Liu, W. C. Wang, J. Luo, X. P. Han, X. W. Du, S. Z. Qiao, J. Yang, *Adv. Mater.* **2018**, *30*, 1800005.
[6] Z. Chen, R. Wu, Y. Liu, Y. Ha, Y. Guo, D. Sun, M. Liu, F. Fang, *Adv. Mater.* **2018**, *30*, 1802011.
[7] A. Kulkarni, S. Siahrostami, A. Patel, J. K. Norskov, *Chem. Rev.* **2018**, *118*, 2302.
[8] Y. Zheng, Y. Jiao, A. Vasileff, S. Z. Qiao, *Angew. Chem., Int. Ed.* **2018**, *57*, 7568.
[9] J. Wang, Z. Wei, S. Mao, H. Li, Y. Wang, *Energy Environ. Sci.* **2018**, *11*, 800.
[10] M. Luo, Z. Zhao, Y. Zhang, Y. Sun, Y. Xing, F. Lv, Y. Yang, X. Zhang, S. Hwang, Y. Qin, J.-Y. Ma, F. Lin, D. Su, G. Lu, S. Guo, *Nature* **2019**, *574*, 81.
[11] X. Peng, T. J. Omasta, E. Magliocca, L. Wang, J. R. Varcoe, W. E. Mustain, *Angew. Chem., Int. Ed.* **2019**, *58*, 1046.
[12] H. Jiang, J. Gu, X. Zheng, M. Liu, X. Qiu, L. Wang, W. Li, Z. Chen, X. Ji, J. Li, *Energy Environ. Sci.* **2019**, *12*, 322.
[13] H. F. Wang, C. Tang, Q. Zhang, *Adv. Funct. Mater.* **2018**, *28*, 1803329.
[14] K. Yuan, C. Lu, S. Sfaelou, X. Liao, X. Zhuang, Y. Chen, U. Scherf, X. Feng, *Nano Energy* **2019**, *59*, 207.
[15] P. Li, Z. Jin, Y. Qian, Z. Fang, D. Xiao, G. Yu, *ACS Energy Lett.* **2019**, *4*, 1793.
[16] R. Gao, Q. Dai, F. Du, D. Yan, L. Dai, *J. Am. Chem. Soc.* **2019**, *141*, 11658.
[17] C. C. Yang, S. F. Zai, Y. T. Zhou, L. Du, Q. Jiang, *Adv. Funct. Mater.* **2019**, *29*, 1901949.
[18] Y. Pan, S. Liu, K. Sun, X. Chen, B. Wang, K. Wu, X. Cao, W. C. Cheong, R. Shen, A. Han, Z. Chen, L. Zheng, J. Luo, Y. Lin, Y. Liu, D. Wang, Q. Peng, Q. Zhang, C. Chen, Y. Li, *Angew. Chem., Int. Ed.* **2018**, *57*, 8614.
[19] T. V. Tam, S. G. Kang, M. H. Kim, S. G. Lee, S. H. Hur, J. S. Chung, W. M. Choi, *Adv. Energy Mater.* **2019**, *9*, 1900945.
[20] Y. Qu, L. Wang, Z. Li, P. Li, Q. Zhang, Y. Lin, F. Zhou, H. Wang, Z. Yang, Y. Hu, M. Zhu, X. Zhao, X. Han, C. Wang, Q. Xu, L. Gu, J. Luo, L. Zheng, Y. Wu, *Adv. Mater.* **2019**, *31*, 1904496.
[21] L. Li, Y. Li, Y. Xiao, R. Zeng, X. Tang, W. Yang, J. Huang, K. Yuan, Y. Chen, *Chem. Commun.* **2019**, *55*, 7538.
[22] Z. Zhang, Y. P. Deng, Z. Xing, D. Luo, S. Sy, Z. P. Cano, G. Liu, Y. Jiang, Z. Chen, *ACS Nano* **2019**, *13*, 7062.
[23] Q. Gao, W. Zhang, Z. Shi, L. Yang, Y. Tang, *Adv. Mater.* **2019**, *31*, 1802880.
[24] K. Yuan, D. Lutzenkirchen-Hecht, L. Li, L. Shuai, Y. Li, R. Cao, M. Qiu, X. Zhuang, M. K. H. Leung, Y. Chen, U. Scherf, *J. Am. Chem. Soc.* **2020**, https://doi.org/10.1021/jacs.9b11852.
[25] Y. Chen, Z. Li, Y. Zhu, D. Sun, X. Liu, L. Xu, Y. Tang, *Adv. Mater.* **2019**, *31*, 1806312.
[26] Y. Deng, B. Chi, J. Li, G. Wang, L. Zheng, X. Shi, Z. Cui, L. Du, S. Liao, K. Zang, J. Luo, Y. Hu, X. Sun, *Adv. Energy Mater.* **2019**, *9*, 1802856.
[27] P. Peng, L. Shi, F. Huo, S. Zhang, C. Mi, Y. Cheng, Z. Xiang, *ACS Nano* **2019**, *13*, 878.
[28] X. Wan, X. Liu, Y. Li, R. Yu, L. Zheng, W. Yan, H. Wang, M. Xu, J. Shui, *Nat. Catal.* **2019**, *2*, 259.
[29] X. X. Wang, D. A. Cullen, Y. T. Pan, S. Hwang, M. Wang, Z. Feng, J. Wang, M. H. Engelhard, H. Zhang, Y. He, Y. Shao, D. Su, K. L. More, J. S. Spendelow, G. Wu, *Adv. Mater.* **2018**, *30*, 1706758.
[30] L. Chen, X. Liu, L. Zheng, Y. Li, X. Guo, X. Wan, Q. Liu, J. Shang, J. Shui, *Appl. Catal., B* **2019**, *256*, 117849.
[31] X. X. Wang, V. Prabhakaran, Y. He, Y. Shao, G. Wu, *Adv. Mater.* **2019**, *31*, 1805126.
[32] L. Bai, C. S. Hsu, D. T. L. Alexander, H. M. Chen, X. Hu, *J. Am. Chem. Soc.* **2019**, *141*, 14190.
[33] Q. Cheng, S. Han, K. Mao, C. Chen, L. Yang, Z. Zou, M. Gu, Z. Hu, H. Yang, *Nano Energy* **2018**, *52*, 485.
[34] H. Xu, J. Cao, C. Shan, B. Wang, P. Xi, W. Liu, Y. Tang, *Angew. Chem., Int. Ed.* **2018**, *57*, 8654.
[35] J. Hou, B. Zhang, Z. Li, S. Cao, Y. Sun, Y. Wu, Z. Gao, L. Sun, *ACS Catal.* **2018**, *8*, 4612.
[36] Q. Xiong, Y. Wang, P. F. Liu, L. R. Zheng, G. Wang, H. G. Yang, P. K. Wong, H. Zhang, H. Zhao, *Adv. Mater.* **2018**, *30*, 1801450.

[37] F. Kong, X. Fan, A. Kong, Z. Zhou, X. Zhang, Y. Shan, *Adv. Funct. Mater.* **2018**, *28*, 1803973.

[38] Z. Yang, C. Zhao, Y. Qu, H. Zhou, F. Zhou, J. Wang, Y. Wu, Y. Li, *Adv. Mater.* **2019**, *31*, 1808043.

[39] M. Zhang, Q. Dai, H. Zheng, M. Chen, L. Dai, *Adv. Mater.* **2018**, *30*, 1705431.

[40] T. Wang, Z. Kou, S. Mu, J. Liu, D. He, I. S. Amiinu, W. Meng, K. Zhou, Z. Luo, S. Chaemchuen, F. Verpoort, *Adv. Funct. Mater.* **2018**, *28*, 1705048.

[41] K. Yuan, X. Zhuang, H. Fu, G. Brunklaus, M. Forster, Y. Chen, X. Feng, U. Scherf, *Angew. Chem., Int. Ed.* **2016**, *55*, 6858.

[42] C. Han, Q. Li, D. Wang, Q. Lu, Z. Xing, X. Yang, *Small* **2018**, *14*, 1703642.

[43] J. Yang, X. Wang, B. Li, L. Ma, L. Shi, Y. Xiong, H. Xu, *Adv. Funct. Mater.* **2017**, *27*, 1606497.

[44] P. Yu, L. Wang, F. Sun, Y. Xie, X. Liu, J. Ma, X. Wang, C. Tian, J. Li, H. Fu, *Adv. Mater.* **2019**, *31*, 1901666.

[45] H. Xu, D. Cheng, D. Cao, X. C. Zeng, *Nat. Catal.* **2018**, *1*, 339.

[46] Q. Cheng, L. Yang, L. Zou, Z. Zou, C. Chen, Z. Hu, H. Yang, *ACS Catal.* **2017**, *7*, 6864.

[47] K. Yuan, S. Sfaelou, M. Qiu, D. Lützenkirchen-Hecht, X. Zhuang, Y. Chen, C. Yuan, X. Feng, U. Scherf, *ACS Energy Lett.* **2018**, *3*, 252.

[48] Y. Zhao, N. Yang, H. Yao, D. Liu, L. Song, J. Zhu, S. Li, L. Gu, K. Lin, D. Wang, *J. Am. Chem. Soc.* **2019**, *141*, 7240.

[49] H. Funke, A. C. Scheinost, M. Chukalina, *Phys. Rev. B* **2005**, *71*, 094110.

[50] H. R. Chauke, D. Nguyen-Manh, P. E. Ngoepe, D. G. Pettifor, S. G. Fries, *Phys. Rev. B* **2002**, *66*, 155105.

[51] D. Xia, X. Yang, L. Xie, Y. Wei, W. Jiang, M. Dou, X. Li, J. Li, L. Gan, F. Kang, *Adv. Funct. Mater.* **2019**, *29*, 1906174.